

Clinton S. Willson,<sup>1</sup> Ning Lu,<sup>2</sup> and William J. Likos<sup>3</sup>

# Quantification of Grain, Pore, and Fluid Microstructure of Unsaturated Sand from X-Ray Computed Tomography Images

**REFERENCE:** Willson, Clinton S., Lu, Ning, and Likos, William J., "Quantification of Grain, Pore, and Fluid Microstructure of Unsaturated Sand from X-Ray Computed Tomography Images," *Geotechnical Testing Journal*, Vol. 35, No. 6, 2012, pp. 1–13, doi:10.1520/GTJ20120075. ISSN 0149-6115.

**ABSTRACT:** A comprehensive series of three-dimensional x-ray computed tomography (XCT) imaging experiments was conducted to quantitatively assess the multiphase particle- and pore-scale properties of fine Ottawa (F-75) sand. The specimens were prepared to saturations ranging from approximately 5 % to 80 %. Specimens were doped with 10 % CsCl pore fluid solution and imaged using a monochromatic synchrotron x-ray source at energies below and above the Cs x-ray absorption k-edge to allow for high contrast between the solid, liquid, and air phases. Multiphase properties quantified from the XCT images included individual particle sizes and areas, as well as grain size distribution, pore shape and size distribution, water menisci distribution, solid, liquid, and gas surface areas, and particle contact coordination number. At low saturations, pore water is distributed primarily in the form of pendular rings and liquid bridges located between individual grains and in the smallest pore throats and bodies. A highly discontinuous water phase is evident as a large number of separately identifiable water units having very small volume. As the water saturation increases, the number of individual water units decreases; as expected, the average volume of these units increases significantly as the pore water coalesces into larger and larger units. Results obtained using SEM imaging and conventional geotechnical testing methods for particle-size distribution and soil–water retention were compared with those derived from analysis of the XCT images. Results compare very well in each case, typically within a few %. It is shown that the XCT is a reliable and non-destructive method to quantify pore-scale information vital to advance understanding of the hydrologic and mechanical behavior of unsaturated soils at the macroscale.

**KEYWORDS:** x-ray computed tomography, unsaturated soil

## Introduction

Micromechanical particle fabric, pore fabric, and fluid distribution in partially saturated soil systems play governing roles in bulk hydrological and mechanical behavior, such as fluid flow, shear strength, and compressibility. The soil–water retention curve (SWRC) and hydraulic conductivity function (HCF) are governing relations for water storage, distribution, and flow and must be quantified for modeling or predicting the hydrologic behavior of unsaturated soil. The SWRC defines the constitutive relationship between soil moisture content and soil suction. The HCF defines the constitutive relationship between soil moisture content and hydraulic conductivity. Both relations are intrinsically related to pore-size distribution, wetting direction, and the types of pore fluid involved, and are highly non-linear functions of saturation. Recent works (Likos and Lu 2004; Lu and Likos 2004; Lu and Likos 2006; Lu et al. 2010a, 2010b) demonstrate through pore-

scale micromechanical considerations and experimental validation that effective stress variations caused by changes in soil suction or moisture content can be quantified by an inter-particle stress function called “suction stress characteristic curve” (SSCC). These works demonstrate the intrinsic relationship between the SWRC, the HCF, and the SSCC, and show that pore size and pore fluid distribution are also fundamental aspects governing the stress-dependent behavior of unsaturated soils, such as strength and compressibility. As a result, there is significant motivation to quantify pore and fluid distribution in partially saturated soil systems and to apply this information for making improved predictions of macroscale flow, strength, and deformation in response to environmental changes.

Quantifying pore and fluid fabric in porous media has historically been experimentally challenging, particularly for systems maintained under undisturbed conditions. For fine-grained soils, mercury intrusion methods have been widely adopted (e.g., Diamond 1970; Sridharan et al. 1971; Romero and Simms 2008); however, uncertainties remain as such methods provide only an indirect measurement of pore-size distribution, do not capture the pore connectivity, and can alter the pore structure during testing. Scanning electron microscopy (SEM), atomic force microscopy (AFM), and environmental scanning electron microscopy (ESEM) continue to provide insight into the fabric features of both coarse-grained and fine-grained soil systems, but such measurements are largely qualitative and in many cases still require special specimen

Manuscript received January 6, 2012; accepted for publication June 29, 2012; published online September 2012.

<sup>1</sup>Louisiana State Univ., Dept. of Civil and Environmental Engineering, Baton Rouge, LA 70803 (Corresponding author), e-mail: cwillson@lsu.edu

<sup>2</sup>Colorado School of Mines, Dept. of Civil and Environmental Engineering, Golden, CO 80401.

<sup>3</sup>Univ. of Wisconsin, Dept. Civil and Environmental Engineering, Madison, WI 53706.

preparation procedures and a testing environment that could be destructive to the pore structure and soil–water interaction processes.

In this paper, we present and evaluate the use of synchrotron x-ray computed tomography (XCT) to non-destructively image and quantify the three-dimensional grain, pore, and fluid structure of fine sand under partially saturated conditions. Grain-based algorithms for identifying grain and pore network structure are described in detail. Quantitative measurements of particle-size distribution, pore-size distribution, the geometry and distribution of water menisci, and air, water, and solid interface areas as functions of saturation are extracted from the tomography images. These image-derived measurements are compared with independent measurements obtained using conventional macroscopic methods. The ability to non-destructively extract these properties provides valuable insights into the role of pore structure on the morphology of the fluid phases in unsaturated soil systems and the pore-level processes that govern corresponding macroscopic behavior.

## X-Ray Computed Tomography

X-ray computed tomography (XCT) provides non-destructive and non-invasive three-dimensional images of the interior of objects by mapping the x-ray attenuation through the specimen. XCT is based on the reconstruction of the cross section of an object from its projection data by passing a series of x-rays through an object, and measuring the attenuation of these x-rays using detectors placed on the downstream side of the object. Projections are obtained by measuring the x-ray attenuation coefficients of the specimen at different angles and then reconstructing into cross sections that give the attenuation values on a pixel basis. These cross sections can then be stacked to give a three-dimensional file of the attenuation values.

In this work, synchrotron-based XCT was used to non-destructively image the samples. Synchrotron radiation has several advantages over traditional x-ray sources, including high photon flux, high degree of collimation, well-defined time structure, and the ability to tune the photon energy over a wide range using an appropriate monochromator for obtaining element- or compound-specific measurements. This feature can be extremely helpful for differentiating fluid phases (e.g., Al-Raoush and Willson 2005a; Prodanovic et al. 2006) or for qualitative identification of mineralogy (e.g., Ketcham 2005). However, a major limitation of synchrotron x-ray sources is the lower operational energies (typically <50 keV compared to a conventional XCT system, which may produce energies over 400 keV), which limit the specimen diameter of typical porous media samples to <1 cm because of higher attenuation at these lower energies (Ketcham and Carlson, 2001; Wildenschild et al. 2002).

At the energies in the typical XCT imaging regime, x-rays are absorbed by all matter through the photo-electric effect. The linear attenuation coefficient,  $\mu$ , gives the probability of x-rays to be absorbed according to Beer's law:

$$I = I_o \exp\left[-\left(\frac{\mu}{\rho}\right)\rho t\right] \quad (1)$$

where  $I$  is the intensity transmitted through the specimen;  $I_o$  is the incident x-ray intensity on a specimen;  $\mu/\rho$  is the mass linear

attenuation coefficient, a function of the incident energy;  $\rho$  is the density or concentration of the element; and  $t$  is the voxel thickness.

The linear attenuation coefficient is a function of the density and atomic number of the specimen and the x-ray energy. If the absorbing material or phase is a chemical compound or mixture, its attenuation coefficients can be approximately evaluated from the coefficients of the constituent elements according to their weighted average. At most energies, the attenuation coefficient is a smooth, decreasing function of energy. However, when the incident x ray has an energy equal to that of the binding energy of a deep core level, there is a sharp increase in absorption corresponding to the promotion of this core level to the continuum (i.e., an absorption edge). Because every atom has core-level electrons with well-defined binding energies, it is possible to select the element to highlight by tuning the x-ray energy to an appropriate absorption edge. Of particular interest to this work is that Cs has an absorption k-edge of 35.98 keV and is soluble in water. Therefore, Cs (in the form of CsCl) can be used to dope the water phase used in these samples, thus providing high-quality data concerning the water-phase content and morphology in unsaturated soil systems containing two fluid phases.

Raw 3D XCT image files contain voxel-specific information on the x-ray attenuation of the material(s) that occupy that particular location. The first major step in analysis is to properly threshold the image so that individual phases can be separated and quantified. The next step is to transform the voxel description of the complex porous system into two parts: (1) individual grains, and (2) a physically representative pore network structure. A number of algorithms have been used for quantitative reconstruction of XCT data (Seidler et al. 2000; Richard et al. 2003; Aste et al. 2004). More recently, Thompson et al. (2006) developed a methodology for particle-scale reconstruction of granular media from which a large amount of morphologic information can be extracted, including parameters obtained by traditional particle-analysis techniques (e.g., particle-size distribution, porosity), as well as in situ parameters not usually available (e.g., spatial correlations in particle size and orientations, particle contacts, particle coordination numbers, and more). The technique, which will be used here, has been successfully applied to relatively uniformly shaped particles, such as spheres, unconsolidated sands, and high-aspect ratio cylinders (Thompson et al. 2006; Reed et al. 2010).

The transformation of the void space from voxels to a pore network should be performed in a way that retains the essential features of the pore structure. There are two general categories of algorithms for extracting pore networks from 3D images: skeletonization algorithms and geometric algorithms. Skeletonization algorithms typically employ a voxel-scale approximation of the medial axis to create a graph of the pore space (e.g., Lindquist et al. 2005). Pores are placed at the nodes of the skeleton and pore throats are defined by the curved elements (voxels) of the skeleton that connect these nodes. This approach has been used to create network structures, calculate permeability, and model multiphase effects, such as capillary pressure curves and relative permeability and other multiphase phenomena on sandstone and carbonate rock

images (Oren and Bakke 2002; Arns et al. 2004; Prodanovic et al. 2006,2007; Thompson et al. 2008).

The other major network generation approach uses some form of geometric analysis to define pore locations, and then builds the network structure from these. Delaunay tessellation-based techniques (Bryant et al. 1993; Thompson and Fogler 1997) have been applied to extract pore structure of packed beds and natural porous media (Al-Raoush et al. 2003; Al-Raoush and Willson 2005a; Thompson et al. 2008), and to study a number of multiphase flow phenomena (Bryant and Blunt 1992; Thompson and Fogler 1997; Gladkikh and Bryant 2003, 2005, 2007). Silin and Patzek (2006) proposed a voxel-based maximum inscribed sphere approach to map pore network structures that was used by Al-Kharusi and Blunt (2007, 2008) to generate networks from tomography image of sandstone and other natural rocks, and modeled two- and three-phase relative permeability and capillary pressure curves. Recently, Bhattacharjee et al. (2011) employed several different image-based network generation algorithms and showed that robust pore network modeling algorithms are not overly sensitive to the specific method of pore network generation provided that the network structure captures the underlying physical and morphologic structure.

The advances in imaging techniques, such as XCT and magnetic resonance imaging, have provided researchers with superior tools to non-destructively characterize the 3D microstructure of granular materials (e.g., Johns et al. 1993; Desrues et al. 1996; Alshibli et al. 2000). The capabilities to characterize the details of individual particles and pore structure of coarse-grained systems, such as sands, have sparked increasing interest in the technology from the geo-engineering community. Computational frameworks have been developed to quantify microstructural features and the complex 3D particle and pore fabric (e.g., Wang et al. 2004). This has led to exciting advances in quantitative interpretation of strain localization phenomena, such as shear banding (Oda et al. 2004; Alshibli and Alramahi 2006; Alshibli and Hasan 2008), asphalt, soil, and rock microstructure (Verhelst et al. 1995; Masad et al. 2002; Wang et al. 2004), pore fluid distribution under transient or steady-state conditions (Wildenschild et al. 2005; Culligan et al. 2006), during multiphase mass transfer (e.g., Schnaar and Brusseau 2005), and the correlation of multiphase fluid distribution and morphology with pore structure (Al-Raoush and Willson 2005b; Prodanovic et al. 2007).

In this work, a methodology to extract pore-level details from XCT images of unsaturated sand systems will be presented and shown to provide quantitative data and valuable insights into the location and morphology of the water phase at various levels of saturation. Absorption-edge imaging using monochromatic synchrotron XCT is used to acquire detailed three-dimensional images that can be segmented into sand, water, and air phases. Characterization of the granular packing provides details on the grain size distribution and grain-grain contacts. Extraction of the pore network structure allows for measurements of the pore and throat sizes, as well as direct mapping of the morphology. Finally, details of the fluid phases, such as volume content and interfacial areas, are calculated, as well as correlations of the fluids with the pore network structure.

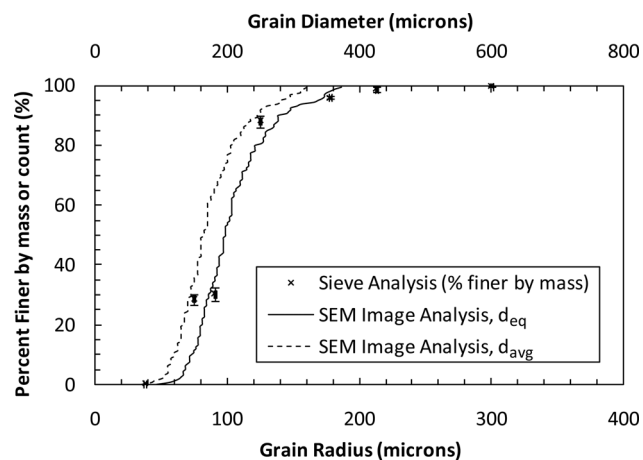


FIG. 1—Grain size distribution curve for F-75 Ottawa sand from mechanical sieve analysis and SEM image analysis.

## Testing Material and Properties

### Grain Size and Morphology

All tests described subsequently were conducted using specimens of F-75 Ottawa sand obtained from the U.S. Silica Company. F-75 Ottawa sand is a poorly graded quartz sand (~99.8 % SiO<sub>2</sub>) with rounded to sub-angular grain morphology. Specific gravity of the mineral solids following ASTM D854-10 was determined to be 2.65. Grain size distribution measured using mechanical sieve analysis (ASTM D422) produced the grain size distribution (GSD) curve shown in Fig. 1. Results shown are the average % finer by mass for three trials of sieve analysis. Vertical error bars indicate maximum and minimum values obtained from the three trials. Coefficients of uniformity ( $C_u$ ) and curvature ( $C_c$ ) from sieve analysis are 1.8 and 1.0, respectively. Median grain diameter by mass  $d_{50}$  is approximately 185  $\mu\text{m}$  (Table 1).

High-resolution images of the sand were acquired using scanning electron microscopy (SEM) to obtain additional quantitative measures of grain shape and grain size distribution. These images (e.g., Fig. 2(a)) were obtained using a FEI Quanta 600 SEM for a thin layer of platinum-sputtered grains spread approximately into a single layer and affixed onto an aluminum mounting stub. Scion image analysis software was used to measure the 2D area ( $a$ ), perimeter ( $p$ ), short axis length ( $d_{\min}$ ), and long axis length ( $d_{\max}$ ) of each particle by manually scribing either a scaled line segment or scaled polygon to each grain identified from the image.

TABLE 1—Summary of grain size characteristics by mechanical sieve analysis and SEM image analysis.

Grain Property	Sieve Analysis (by mass)	Image Analysis, $d_{eq}$ (by count)	Image Analysis, $d_{avg}$ (by count)
$d_{60}$ ( $\mu\text{m}$ )	200	206	170
$d_{50}$ ( $\mu\text{m}$ )	185	196	165
$d_{30}$ ( $\mu\text{m}$ )	150	171	145
$d_{10}$ ( $\mu\text{m}$ )	110	146	120
$C_u$	1.8	1.4	1.4
$C_c$	1.0	1.0	1.0

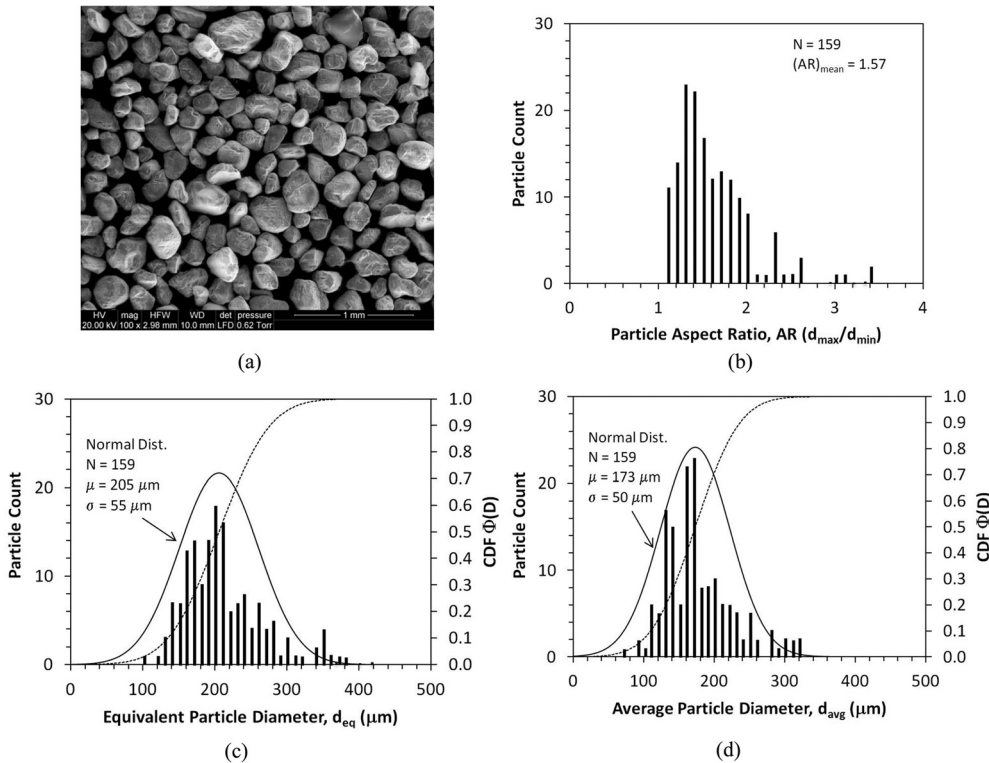


FIG. 2—SEM image analysis of grain size and shape distribution: (a) SEM image, (b) aspect ratio distribution, (c) equivalent particle diameter ( $d_{eq}$ ) distribution, and (d) average particle diameter ( $d_{avg}$ ) distribution.

Distributions of particle aspect ratio (AR), equivalent particle diameter ( $d_{eq}$ ), and average particle diameter ( $d_{avg}$ ) defined as

$$AR = \frac{d_{max}}{d_{min}} \quad (2)$$

$$d_{eq} = \frac{p}{\pi} \quad (3)$$

$$d_{avg} = \frac{d_{min} + d_{max}}{2} \quad (4)$$

$$I_{sph} = \frac{1}{N} \sum_{i=1}^N \frac{d_{eq(i)}}{d_{min(i)}} - \frac{d_{eq(i)}}{d_{max(i)}} \quad (5)$$

were obtained from these measurements. Figures 2(b) through 2(d) show corresponding histograms for the particle population identified in Fig. 2(a) ( $N=159$ ). Values derived from these distributions are also summarized in Table 1 for comparison with those derived from mechanical sieve analysis. Sphericity index ( $I_{sph}$ ) calculated for the population following Eq 5 (Alsaled 2004) was determined to be  $I_{sph}=0.53$ , where a value of  $I_{sph}=0$  indicates a perfect sphere.

### Soil–Water Retention Curves

Soil–water retention curves (SWRC) were determined for the F-75 sand using a combination of axis translation (Tempe cell) and hanging column techniques (ASTM D6836-02). Air-dried sand specimens were first compacted to an average initial porosity ( $n_p$ ) of 0.401, saturated in a vacuum dessicator, and then tested in Tempe pressure cells along a drainage path. Three trials were conducted using the Tempe cell (TC) method ranging from matric

suction of 0 kPa to a maximum near 75 kPa. One trial was conducted using the hanging column (HC) method for a specimen compacted to similar porosity ( $n_p=0.412$ ) and for matric suction ranging from 0 kPa to a maximum of near 5 kPa. Figure 3 shows retention curves for the three TC trials and the one HC trial. These data were fit using van Genuchten's (1980) model,

$$S_e = \frac{S - S_r}{1 - S_r} = \frac{\theta - \theta_r}{\theta_s - \theta_r} = \left[ \frac{1}{1 + (\alpha\psi)^n} \right]^m \quad (6a)$$

where  $S_e$  is the effective saturation,  $\theta_r$ , the irreducible water content,  $S_r$ , the irreducible water saturation, and the fitting parameters

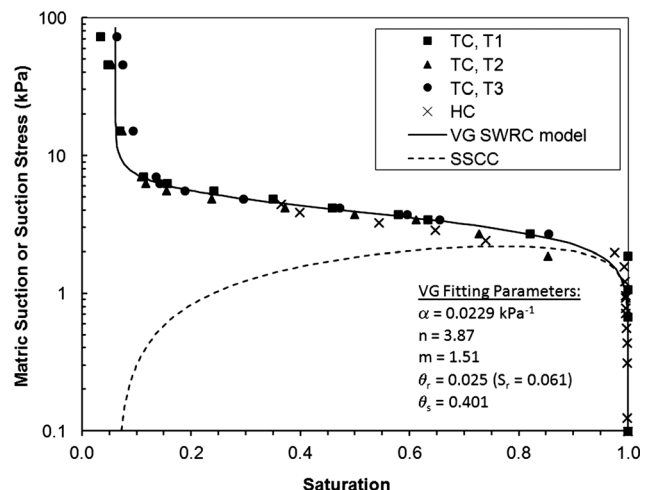


FIG. 3—Water retention curves for the three TC trials and the one HC trial.

TABLE 2—Summary of grain information from XCT analysis.

Sample	Porosity	No. Grains	Ave. GV ( $\times 10^7$ mm $^3$ )	Ave. GIR (mm)	Ave. GAR	Ave. GSA ( $\times 10^6$ mm $^2$ )	Grain SSA (l/cm)	Ave. GCN
CSM2	0.428	6232	0.40	64.30	1.62	0.11	154.19	6.19
CSM3	0.417	6058	0.42	65.60	1.61	0.11	148.50	6.60
CSM4	0.427	6464	0.39	64.00	1.61	0.10	152.52	6.81
CSM5	0.377	6757	0.40	64.60	1.62	0.10	159.44	7.52
CSM6	0.392	6965	0.38	62.90	1.64	0.11	167.54	7.45
CSM7	0.390	7063	0.38	62.80	1.62	0.10	168.28	7.41
CSM8	0.366	7151	0.39	64.10	1.61	0.10	165.46	7.77
CSM9	0.372	6915	0.40	63.70	1.62	0.11	171.09	7.72
CSM10	0.412	7035	0.37	62.00	1.64	0.11	169.22	7.27

Note: GV, grain volume; GIR, grain inscribed radius; GAR, grain aspect ratio; GSA, grain surface area; SSA, specific surface area; GCN, grain coordination number.

( $\alpha$ ,  $n$ ,  $m$ ) are optimized by least-squared regression. The corresponding suction stress characteristic curve (SSCC) for the sand is plotted in Fig. 3 from the closed form solution (Lu and Likos 2004, 2006; Lu et al. 2010a):

$$\sigma^s = \frac{S_e}{\alpha} \left[ (S_e)^{\frac{n}{1-n}} - 1 \right]^{1/n} \quad (6b)$$

where suction stress ( $\sigma^s$ ) quantifies effective stress arising from matric suction for partially saturated soils and the SSCC defines the relationship between suction stress and saturation. Suction stress represents the sole effective stress change under varying saturation conditions for all types of soils. As noted in Fig. 3, the SSCC for the sand shows non-monotonic behavior with an up-and-down response typical of that for coarse-grained soils (Lu et al. 2007, 2009). This up-and-down behavior in the SSCC is subsequently shown to reflect similar behavior in the relationship between capillary air–water interface area and saturation determined via XCT imaging.

### Specimen Preparation and XCT Imaging Procedures

A series of nine Ottawa sand specimens were prepared by mixing dry sand with water doped with CsCl at 10 % by weight to produce different saturations at target porosity of 0.390. Saturation ranged from a minimum of 5 % to a maximum near 85 %. Small cylindrical specimens were prepared for scanning following several steps. Approximately 100 g of dry sand was mixed with the amount of CsCl-doped water necessary to achieve the target water content. The mixture was then cured overnight in an airtight glass jar and a sub-specimen was taken to calculate water content after homogenization. The mixture was then compacted into a thin-walled (wall thickness = 0.36 mm) aluminum tube with a 10-mm inner diameter and 10-mm length for placement on the scanning stage. Moisture content measured from the sub-specimen and mass–volume relationships for the compacted specimen were used to calculate final porosity and degree of saturation. The porosities of all nine specimens prepared in such manner are shown in Table 2, and the moisture contents in Table 4. Average porosity achieved for the XCT specimens was 0.398 with a standard deviation of 0.024. The favorable comparison between target porosities achieved for the XCT specimens ( $n_{p-\text{avg}} = 0.398$ ) and

the Tempe cell and hanging column specimens ( $n_{p-\text{avg}} = 0.406$ ) was considered sufficient for making direct comparisons between water retention characteristics measured at the particle scale and the macroscale. The sand specimens were all imaged using absorption edge synchrotron XCT at the GeoSoilEnviroCARS (GSECARS) 13-BM-D beamline at the Advanced Photon Source, Argonne National Laboratory. The same imaging procedure was used for all the specimens. The column was mounted atop the tomography specimen rotation stage using a chuck and a total of 720 projection images were collected as the specimen was rotated from 0° to 179.5° by 0.5°, then 0.25° to 179.75° by 0.5°. Over the course of the imaging experiment, the incident x-ray flux was stabilized to within a few % by operation in “top-up mode.” Image reconstruction, the process of converting 2D projection images into a 3D volumetric file, was performed using filtered back-projection algorithms developed by GSECARS (Rivers, <http://cars9.uchicago.edu/gsecars/index.html>). Each voxel in the 3D volumetric data file (650 × 650 × 512 voxels) contains a linear attenuation value that depends upon the composition of the phases and the x-ray energy. The voxel sizes in all of the reconstructed images ranged between 10.9 and 11.15  $\mu\text{m}$ .

As mentioned previously, the water in these systems was doped with CsCl at 10 % by weight and the Cs x-ray absorption k-edge is 35.985 keV. To provide a sharp contrast between the three phases (i.e., solid, water, and air), each column was imaged at two energies: one below the Cs x-ray absorption k-edge and a second energy above. At the below k-edge energy, the x-ray absorption of the doped water is well below that of the solid, which allows for high contrast between the solid and void regions. At the above k-edge energy, the CsCl-doped water phase becomes highly absorbing and allows for a clear separation of the water from the air and solid. Because the below- and above-edge energies are close, the x-ray absorption of the solid (sand) and air phases remain essentially constant. Thus, subtraction of the two images gives a difference image where only the CsCl-doped water voxels have non-zero attenuation values. This procedure allows for highly detailed segmentation of the water phase.

Before segmenting the images into the three phases (solid, water, and air), sub-volumes ( $350^3$  voxels) were extracted from the original image volumes. These sub-volumes are from regions within the column that are at least one grain diameter from the column walls, removing most wall (boundary) effects. The resulting

3D images were then segmented using an indicator kriging (IK) based technique first developed by Oh and Lindquist (1999) and then modified as described in Bhattacharjee et al. (2010). In the IK approach, the segmentation is based on two threshold values, T1 and T2; intensity values below the lower threshold value, T1, are identified as phase one and intensity values larger than the higher threshold value, T2, are identified as phase two. Values between the two threshold values are assigned to either phase using the maximum likelihood estimate of each phase based on the two-point correlation function. Each segmentation trial is evaluated both quantitatively (e.g., porosity, water saturation) and qualitatively (i.e., comparison of segmented image to the original grayscale) to select the final segmented image to be used for further analysis. For each of the systems tested, the below-edge image was used to separate the solid phase from the void space, whereas the difference image was used to identify the voxels occupied by the water phase. Finally, the two segmented images were combined to create a single volume file where each voxel contained a unique integer value corresponding to one of the three phases (e.g., 0 = solid, 1 = water, and 2 = air). The image voxel resolution used here ( $\sim 11 \mu\text{m}$ ) is sufficient to provide quantitative data on the grains (Thompson et al. 2006) and the use of absorption edge imaging is similar to previous work on similar media and fluids (Al-Raoush and Willson 2005a, 2005b; Schnaar and Brusseau 2005; Wildenschild et al. 2005) that have demonstrated the ability to extract the pore structure and/or quantify the pore-level fluid properties.

## Algorithm for Grain and Pore Network Structure Identification

The grain-based approach for network generation in a granular media is a two-step process: (1) computationally reconstruct particles from the XCT image, and (2) use the particulate structure as a template to create the pore and pore-throat network. The rationale for this approach is that pores are formed by clusters of grains or particles in an unconsolidated granular material. Thus, using particle locations as a template ensures that the correct characteristic scale is used to define the pore structure. The following is a summary of the algorithms used to extract individual grains, packing properties and pore network structure. Additional details can be found in Thompson et al. (2006, 2008) or at [www.poresim.org](http://www.poresim.org).

The grain reconstruction step is performed by an algorithm called “vox2grains” (Thompson et al. 2006). It transforms a binary image (e.g., solid-phase voxels equal 0, void-phase voxels equal 1 or 2) into a grain-scale map in which each solid-phase voxel is tagged with the grain number to which it belongs. The algorithm uses a combination of erosion followed by non-linear optimization to search for the maximal inscribed sphere that is contained inside each grain. Once the grain centers are located (i.e., the locations of the maximal inscribed spheres, not the centers of mass of the grains), voxels belonging to that particular grain are collected from the center moving outward using a variant of the watershed algorithm. Once every solid-phase voxel is tagged with its respective particle number, any particle or grain in the packing can be reconstructed from the digital image simply by

retrieving the corresponding cluster of voxels. This approach allows a number of physical properties of the material to be computed, including total particle surface area, number of grain–grain contacts and the surface area of these contacts (limited by voxel resolution), grain volumes, grain orientations, grain locations, grain aspect ratios, and, if multiple fluid phases are present, fraction of surface areas exposed to each fluid (Thompson et al. 2006).

The second step in the grain-based network-generation process is to create the pore and pore-throat map (i.e., physically representative pore network structure) of the void space using the granular structure of the material as a template. For sphere packings and other materials made from compact grains, clusters of four or more particles create pores in the void structure. This same particle cluster that forms a pore also has smaller gaps in its shell that lead into and out of the central pore (i.e., pore throats). Hence, using the granular structure as a template for the network structure is a more physically appealing approach than working directly from the voxel map itself. As mentioned previously, Delaunay tessellation and a modified form have been used by others to transform the continuous, interconnected void space in a sphere packing into a discrete set of pores and pore throats. In this work, the modified Delaunay tessellation (MDT) approach is used in an implementation that operates on voxel images. Parameters that describe the pore network include inscribed pore radii (i.e., the radius of the largest sphere that can be placed in the pore), pore volumes, throat radii, throat cross-sectional areas, throat surface areas, throat-wetted perimeters, throat hydraulic conductances, and the connectivity of the network itself (Thompson et al. 2008; Bhattacharjee et al. 2011).

Analysis of the fluid phase is performed as follows. The first voxel that is identified as containing the fluid phase of interest (in this case, water) is labeled and then a connected component algorithm is used to label all connected voxels that contain water. Once the algorithm has found all of the connected voxels and has labeled them with the same integer (e.g., 1), the program finds another water-containing voxel that was not identified in the previous step, labels that voxel with another integer (e.g., 2) and identifies and labels the voxels connected to that one. This procedure is continued until all of the water-filled voxels have been identified, grouped with the connected voxels, and labeled. At this point, it is trivial to collect properties of the individual fluid “units,” such as volume, orientation, surface area (both fluid–fluid and fluid–solid) as well as correlate the location of each unit to the pore network structure.

## Testing Results

After segmentation, each of the image files contains voxels that are assigned to one of the three phases, solid, water, or air. Qualitatively, these images (Figs. 4 and 5) show that, as expected, at low volumetric contents the water is distributed primarily in the form of pendular rings and bridges and appears to be discontinuous. In reality, the water is also present in these systems as films that coat the sand particles. However, the resolution of these images does not allow for the films to be seen. As the water

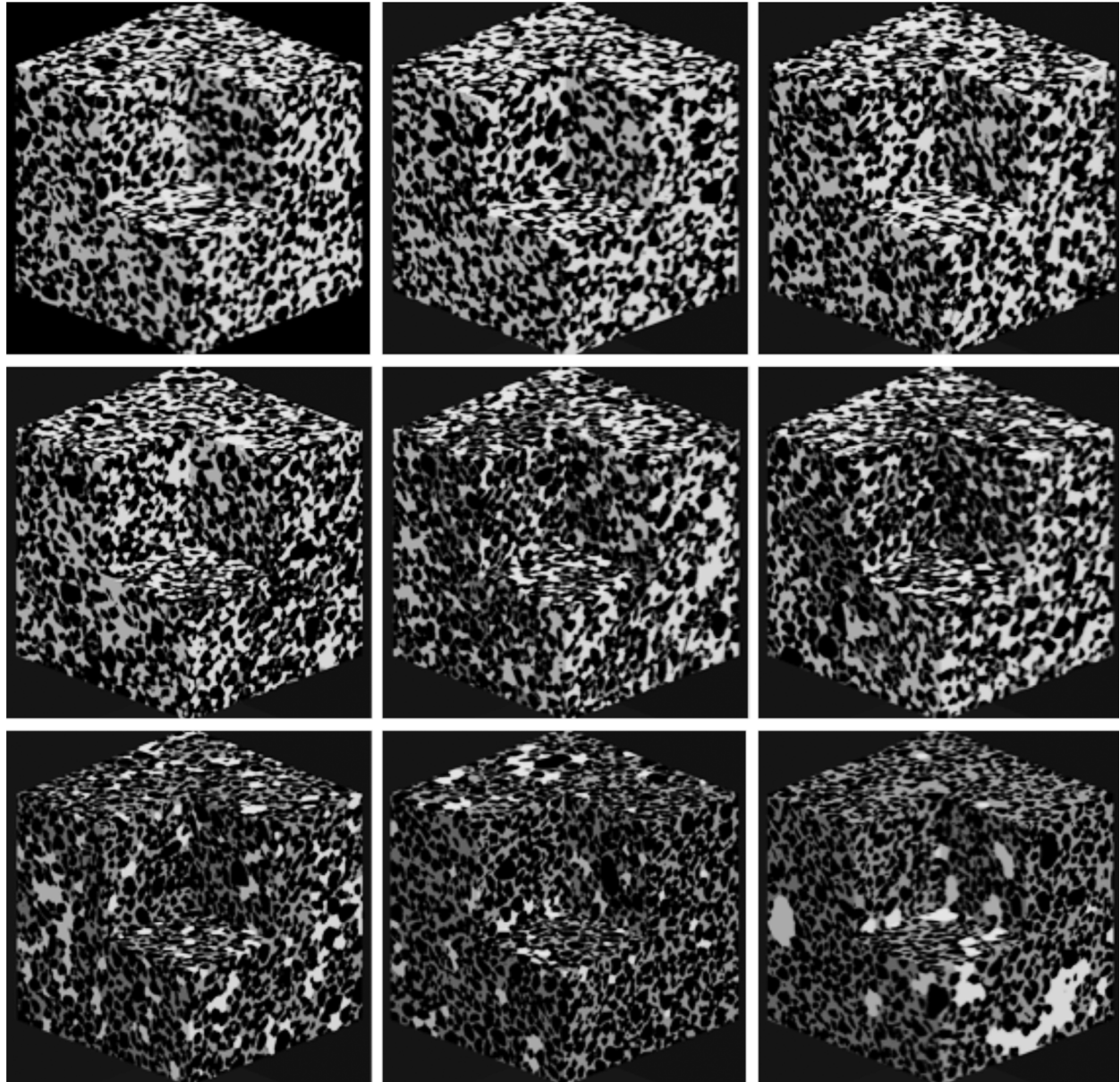


FIG. 4—Segmented images of the nine specimens at varying degrees of volumetric water content. Cubes are  $350^3$  voxels with each side  $\sim 3.85$  mm in length. CSM 2–4 (top row); CSM 5–7 (middle row); and CSM 8–10 (bottom row). Black: sand; gray: water; and white: air.

content increases, a majority of the pore space fills with water and the air becomes trapped as a truly discontinuous phase.

Data from the grain-based algorithm can be used to check that the soil/void segmentation is correct and also correlate bulk properties, like the porosity, to grain-level details. Minor differences in segmentation values can produce measurable differences in porosity that may or may not be real. However, identification and measurement of the individual grains in each image and the bulk grain statistics allows us to ensure that the segmentation has produced similar grain-level properties (e.g., average grain inscribed radius, average grain volume) over all the specimens. So, whereas the porosity of the nine systems imaged vary from 0.366 to 0.428, the statistics concerning the individual grains (Table 2), such as grain volume (GV), grain inscribed radius (GIR), grain aspect

ratio (GAR), and average grain surface area (GSA) show very good consistency from one specimen to another. Thus, we can conclude that the solid/void segmentation in all of the images is correct. A plot of the grain effective diameter (GED) distribution (Fig. 6) also highlights the similarity between grain sizes identified from images for the multiple sub-specimens. Comparison with the grain size distribution (GSD) estimated by 2D analysis of the SEM image is only fair, because of the simplistic nature of the calculation. It can also be gleaned from Table 2 that there is a direct correlation between the porosity and the grain–grain details. The most obvious comparison can be seen by looking at the details for CSM4 and CSM8, which have nearly identical grain properties, but porosities of 0.43 and 0.37, respectively. The differences in the detailed packing properties can be quantified by

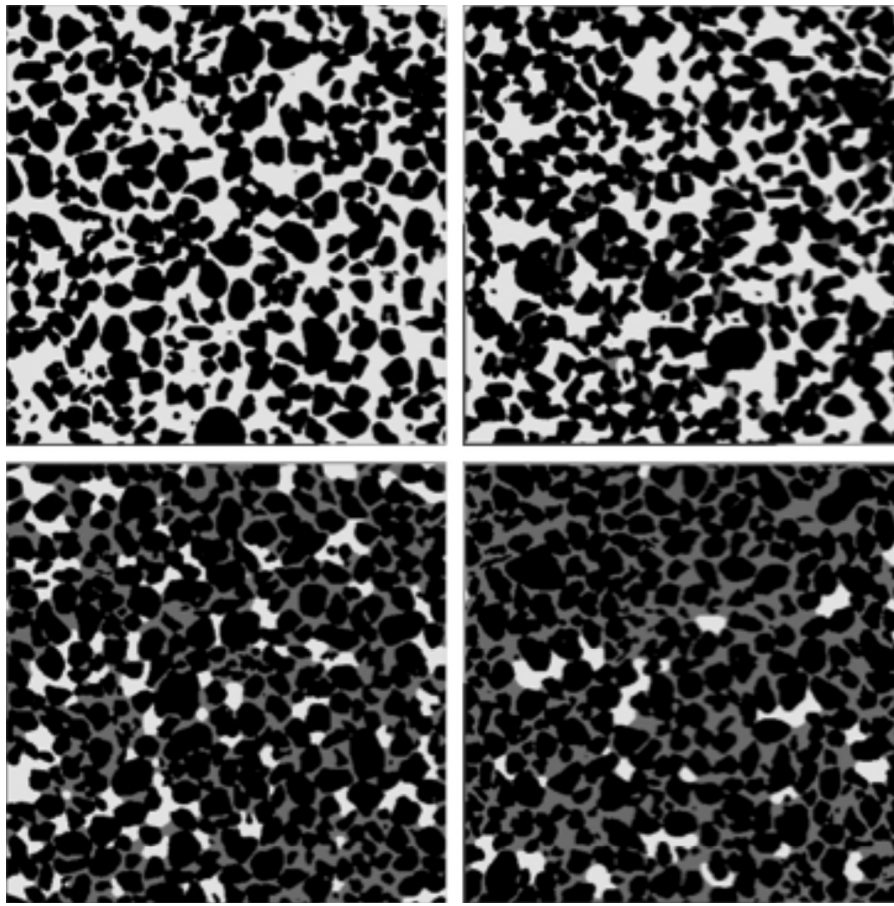


FIG. 5—Representative cross sections from four of the system: CSM2 (upper left); CSM5 (upper right); CSM7 (bottom left); and CSM9 (bottom right). Cross sections are 350° with each side ~3.85 mm in length. Black: sand; gray: water; and white: air.

comparing the number of grains contained in the analyzed sub-volume, which remain the same size in all the specimens, the average grain coordination number, and the grain (i.e., solid/void) specific surface area (grain SSA). As expected, the system with the lower porosity (CSM8) has a larger number of grains within the sub-volume and thus, a larger grain SSA. In addition, the average number of grain–grain contacts in the lower porosity, tighter packed system, CSM8, is higher than CSM4. Whereas not the

focus of this study, differences in the number of grain–grain contacts can have an important effect on the geomechanic and acoustic properties of porous systems (e.g., Reed et al. 2010).

In addition to generating a three-dimensional map of the physically representative pore space, the details of pore network structure provide an easy means of generating pore statistics and pore connectivity (Table 3). In general, the data show a fairly high degree of consistency between the nine specimens indicating that the packing and pore structure differences should not have a major

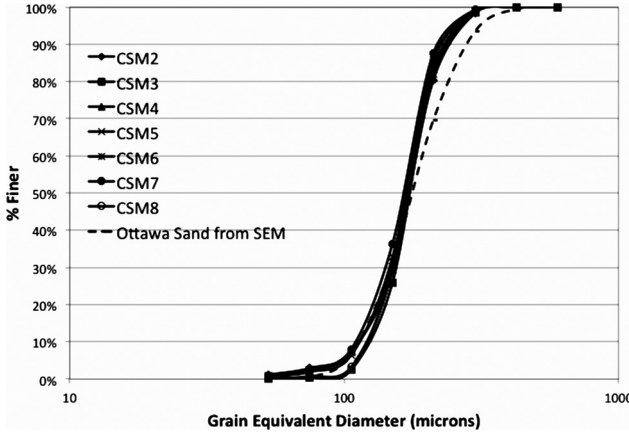


FIG. 6—Equivalent grain diameter distributions for different specimens from the XCT analysis and SEM image analysis for the Ottawa sand.

TABLE 3—Summary of pore information from XCT analysis.

	Number of Pores	Ave. PIR (mm)	Ave. PCN	Ave. TIR (mm)	Ave. PTAR
CSM2	26090	35.40	5.83	25.90	0.68
CSM3	24898	35.50	5.50	26.30	0.68
CSM4	26358	34.40	5.50	25.60	0.68
CSM5	30768	31.60	5.29	23.60	0.70
CSM6	32111	31.00	5.55	22.90	0.69
CSM7	32453	31.10	5.59	22.80	0.69
CSM8	34369	29.60	5.27	22.20	0.7
CSM9	34446	29.30	5.52	21.60	0.7
CSM10	33179	30.40	5.75	22.20	0.69

Note: PIR, pore inscribed radius; PCN, pore coordination number; TIR, throat inscribed radius; PTAR, pore-throat aspect ratio.

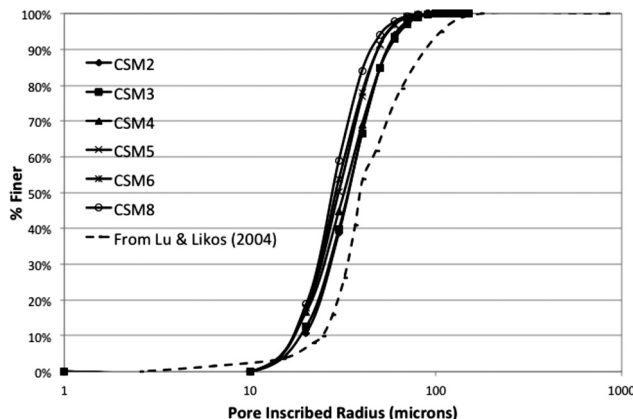


FIG. 7—Comparisons of pore-size distributions obtained from XCT images and estimated from the soil–water retention curve (Lu and Likos 2004).

impact on the fluid distribution and characteristics. A closer inspection, however, shows some correlation between the packing and the pore structure. For example, the pore and throat sizes (pore inscribed radius, PIR and throat inscribed radius, TIR, respectively), as well as the pore coordination number, PCN, are all smaller for the systems with the lower porosity (e.g., CSM8) than for the higher porosity (e.g., CSM 4). The cumulative pore-size distribution plot (Fig. 7) also shows a consistency between specimens with some minor differences because of packing. Figure 7 also includes a pore-size distribution (PSD) indirectly calculated from the experimental water retention results (Fig. 3) using the general procedures with an assumed cylindrical pore geometry described in Lu and Likos (2004). Whereas the general features of the PSDs are comparable, pore sizes predicted from the SWRC using the cylindrical pore assumption are approximately two times larger than the imaged pore sizes.

Volumetric water content values calculated from the segmented images ( $\theta$  imaged) show very good agreement with those measured gravimetrically ( $\theta$  gravimetric). The absolute difference between  $\theta$  imaged and  $\theta$  gravimetric for the nine specimens (Table 4) is not greater than 0.023 and averages 0.010. The most likely reasons for the small discrepancy include the limited capacity for water in the form of thin films to be resolved in the CT images and the fact that only a sub-volume of each specimen was imaged and analyzed, whereas the gravimetric lab

measurements give the total water content in the entire specimen. With the exception of only the driest specimen (CSM2),  $\theta$  imaged is less than  $\theta$  gravimetric for water contents up to about 0.15 (CSM6). Underestimation of water content from the XCT images reflects the inability for tightly adsorbed water films to be resolved from the images in the low saturation regime. The % difference between  $\theta$  imaged and  $\theta$  gravimetric is also largest for specimens prepared at the lower water contents and generally decreases with increasing water content. Average % difference for the nine specimens is 11.8 %.

At low volumetric content the water is distributed primarily as pendular rings and as bridges located at the grain–grain contacts and in the smallest pores and throats. Whereas this water is connected via thin films, the XCT images do not capture the films and therefore, the total number of individual water units (Table 4) is highest at the lowest water contents. As the volumetric content increases and the films swell, the water becomes more directly connected (and able to be imaged) resulting in a decrease in the number of units and an increase in the number of pores occupied. The average volume of individual water units or “blobs” and their corresponding surface area (Table 4) also increase with increasing saturation, reflecting the larger volume of fully connected water units.

Mapping of the location of the water phase and the pore network structure allows for a one-to-one correlation of the pores that are filled with water (Figs. 8(a)–8(d)). The total height of each bar indicates the percentage of the total number of pores of a particular size range. The unfilled region in each bar indicates the fraction of those pore sizes filled with water. At low water contents (Figs. 8(a) and 8(b)), the water is located only in the smallest pores and fills only a fraction of those pores. As the water content increases, corresponding to lower capillary pressure values, the water fills nearly all of the smaller pores and invades the larger pores (Figs. 8(c) and 8(d)).

Surface areas for all three phases are calculated from the segmented images (Table 2 for grain and Table 4 for water). From these values, the specific surface areas (SSA) were calculated and then plotted as a function of water content (Fig. 9). Whereas the grain SSA (SSA\_grain) is relatively consistent throughout, there is some variability because of changes in system packing. At the very lowest water contents, the air phase SSA (SSA\_air) is close to, but always less than, the grain-phase SSA because of the

TABLE 4—Summary of water content, morphology (distribution) and related properties from the XCT analysis.

	S_water (image)	$\theta$ _water (image)	$\theta$ _water (gravimetric)	No. Units	Pores Occupied	Ave. blob vol. ( $\times 10^5$ mm $^3$ )	Ave. blob surface area ( $\times 10^5$ mm $^2$ )	Total water/air SSA (l/cm)
CSM2	0.065	0.028	0.020	3936	0.143	0.66	0.14	153.9
CSM3	0.072	0.030	0.036	4494	0.44	1.4	0.24	140.2
CSM4	0.126	0.054	0.062	3166	1.93	5.86	0.78	126.3
CSM5	0.167	0.063	0.074	3171	2.36	6.8	0.89	127.8
CSM6	0.400	0.157	0.149	867	20.83	75.2	6.7	85.8
CSM7	0.428	0.167	0.153	749	24.6	92.99	8.06	83.7
CSM8	0.705	0.258	0.247	112	261.6	240	65.3	36.5
CSM9	0.796	0.296	0.292	18	1761	7138	420.8	22.8
CSM10	0.840	0.346	0.323	14	2309	10750	551.7	12.8

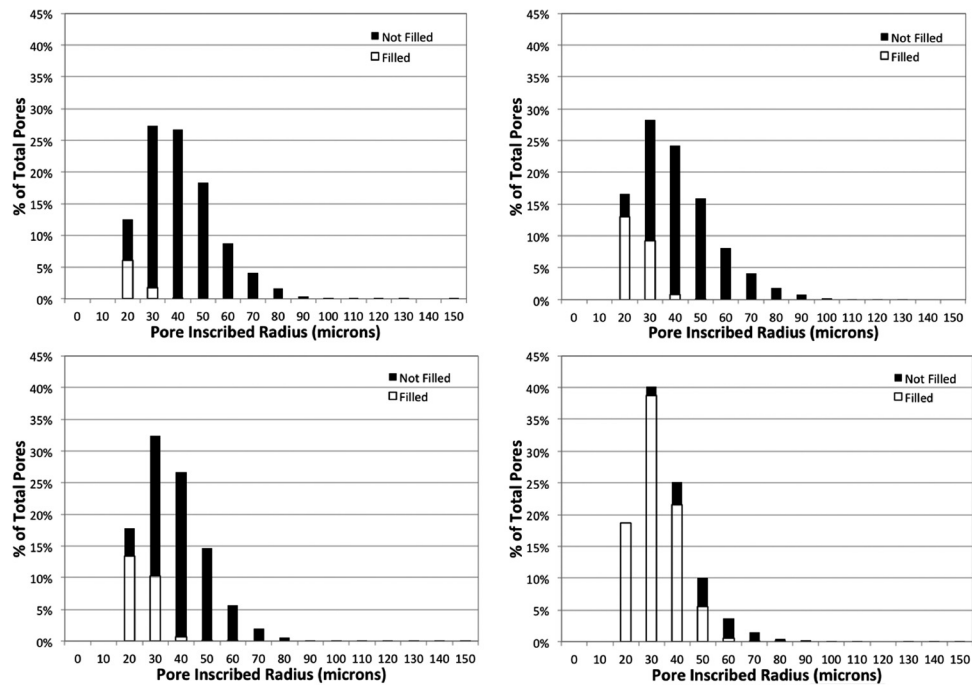


FIG. 8—Pore air and pore water distributions from XCT analysis: upper left (CSM3); upper right (CSM4); lower left (CSM5); and lower right (CSM8).

presence of the water only in the smallest pore bodies and throats and as pendular rings. As expected, the air-phase SSA decreases and the water-phase SSA (SSA\_water) increases as the water content increases.

The capillary water SSA (SSA\_capwater) is a measure of the interfacial area between the non-film water phase and air and is calculated from the three SSA values presented previously following the method described by Dalla et al. (2002). As can be seen in Fig. 9, the capillary water SSA increases from dry to low-level water saturations, plateaus within the mid-range saturations, and then decreases at the highest values. The occurrence of a peak interface area between about 20 % and 50 % saturation is in very good agreement with previous pore-scale model simulations and tomography-based measurements (e.g., Reeves and Celia 1996; Dalla et al. 2002; Culligan et al. 2006) and with the Monte Carlo simulation-based calculations performed on these same systems

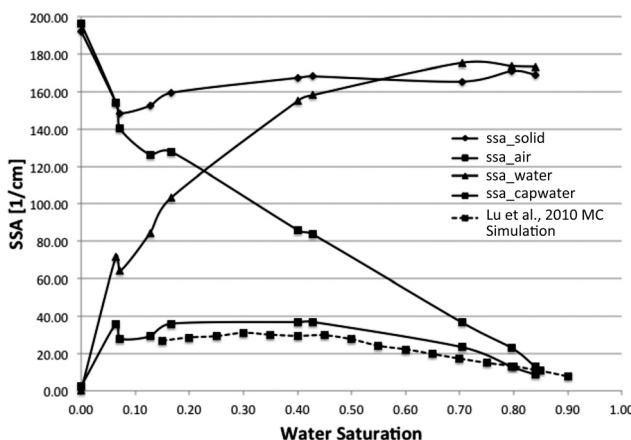


FIG. 9—Specific surface areas (SSAs) as a function of water saturation.

(Lu et al. 2010b) that are also shown on Fig. 9. As conceptualized in the SSCC (Lu and Likos 2006), capillarity or surface tension is the main mechanism responsible for interparticle stress in sand. Therefore, the interfacial area between air and water should completely control the suction stress in sand. The fact that the non-monotonic pattern of the SSCC deduced from the SWRC shown in Fig. 3 follows with the air–water interface area shown in Fig. 9 confirms the notion that the interface area controls the SSCC in sand.

## Summary and Conclusions

Grain- and pore-level distributions and relationships between water and soil play an important role in hydrologic and mechanical processes in unsaturated soils. Many of the constitutive relations currently employed to model or predict these behaviors are either empirically determined or based on fundamental processes on idealized systems. Recent advances in non-destructive 3D XCT now provide the means for extracting the micro-level details in many natural systems.

Here, we have presented results from a series of imaging experiments covering a range of volumetric water contents in partially saturated F-75 sand. Nine sub-specimens were doped with 10 % CsCl pore fluid solution and imaged using a monochromatic synchrotron x-ray source at energies below and above the Cs x-ray absorption k-edge to allow for high contrast between the solid, liquid, and air phases. Methodologies to extract pore-level details from the XCT images provide quantitative data on the location and morphology of the water phase at various levels of saturation.

Reconstructed XCT images show that at volumetric contents corresponding to saturations less than approximately 15 %, the pore water in the sand is distributed primarily in the form of

pendular rings and liquid bridges located between individual grains. A highly discontinuous water phase is evident as a large number of separately identifiable water units having very low volume. At higher saturations, the number of individual water units decreases; however, the average volume of the individual units increases significantly as the pore water coalesces into larger and larger units. At high water saturations, a majority of the pore space is filled with water and the air becomes trapped as a truly discontinuous phase. Mapping of the location of the water phase and the pore network structure allows for a one-to-one correlation of the pores that are filled with water. At low water contents, the water is located only in the smallest pores and fills only a fraction of those pores. As water content increases, the water fills nearly all of the smaller pores and invades the larger pores.

Volumetric water content values calculated from the XCT images show very good agreement with values measured using a conventional macroscopic gravimetric approach. Water content from the images is generally underestimated by comparison with gravimetric measurements for volumetric water contents less than about 0.15, corresponding to saturation of less than about 37 %, an observation attributed to inability of water in the form of thin films to be resolved in the XCT images. The % difference between image-based and measurement-based water generally decreases with increasing water content and averages 11.8 % for the nine specimens. Statistics concerning the individual grains such as grain volume (GV), grain inscribed radius (GIR), grain aspect ratio (GAR), and average grain surface area (GSA) show very good consistency among the nine sub-specimens.

Surface areas calculated from the images as a function of saturation show that the solid phase surface area is relatively consistent, although there is some variability because of variations in system packing among the nine specimens. At very low water contents, the air-phase surface area is close to, but always less than, the solid-phase surface area because of the presence of the water only in the smallest pore bodies and throats and as pendular rings. The air-phase surface area decreases and the water-phase surface area increases as the water content increases. Capillary water surface area, quantifying the interfacial area between the non-film water phase and air, increases from dry to low-level volumetric contents, plateaus within the mid-range contents, and then decreases at the highest values. The fact that the non-monotonic pattern of the SSCC echoes the air–water interface area confirms the notion that the interface area controls the SSCC in sands. Future work should be directed to explore the quantitative linkage between the interfacial area and the SSCC of unsaturated sands.

### Acknowledgments

The imaging work was performed at GeoSoilEnviroCARS (Sector 13), Advanced Photon Source (APS), Argonne National Laboratory. GeoSoilEnviroCARS is supported by the National Science Foundation - Earth Sciences (EAR-1128799) and Department of Energy - Geosciences (DE-FG02-94ER14466). Use of the Advanced Photon Source was supported by the U. S. Department of Energy, Office of Science, Office of Basic Energy Sciences, under Contract No. DE-AC02-06CH11357. This material is based

upon work partially supported by the National Science Foundation (NSF) under Grant No. CMMI 0856276 to W.J.L. Any opinions, findings, and conclusions or recommendations expressed in this material are those of the authors and do not necessarily reflect the views of the National Science Foundation. The partially saturated Ottawa sand specimens for the XCT images were prepared by Dr. Alexandra Wayllace. Her assistance is greatly appreciated.

### References

- Al-Kharusi, A. S. and Blunt M. J., 2007, "Network Extraction from Sandstone and Carbonate Pore Space Images," *J. Pet. Sci. Eng.*, Vol. 56, No. 4, pp. 219–231.
- Al-Kharusi, A. S. and Blunt M. J., 2008, "Multiphase Flow Predictions from Carbonate Pore Space Images Using Extracted Network Models," *Water Res. Res.*, Vol. 44, No. 6.
- Al-Raoush, R. I. and Willson, C. S., 2005a, "Extraction of Physically Realistic Pore Network Properties from Three-Dimensional Synchrotron X-Ray Microtomography Images of Unconsolidated Porous Media Systems," *J. Hydrol.*, Vol. 300, No. 10, pp. 44–64.
- Al-Raoush, R. I. and Willson, C. S., 2005b, "A Pore-Scale Investigation of a Multiphase Porous Media System," *J. Contam. Hydrol.*, Vol. 77, pp. 67–89.
- Al-Raoush, R., Thompson, K., and Willson, C. S., 2003, "Comparison of Network Generation Techniques for Unconsolidated Porous Media," *Soil Sci. Soc. Am. J.*, Vol. 67, pp. 1687–1700.
- Alsaleh, M. I., 2004, "Numerical Modeling of Strain Localization in Granular Materials Using Cosserat Theory Enhanced with Microfabric Properties," Ph.D. dissertation, Louisiana State University, Department of Civil and Environmental Engineering, Baton Rouge, LA, 190 pp.
- Alshibli, K. and Alramahi, B., 2006, "Microscopic Evaluation of Strain Distribution in Granular Materials During Shear," *J. Geotech. Geoenviron. Eng.*, Vol. 132, No. 1, pp. 80–91.
- Alshibli, K. and Hasan, A., 2008, "Spatial Variation of Void Ratio and Shear Band Thickness in Sand Using X-Ray Computed Tomography," *Geotechnique*, Vol. 58, No. 4, pp. 249–257.
- Alshibli, K., Sture, S., Costes, N. C., Frank, M. L., Lankton, M. R., Batiste, S. N., Swanson, R. A., 2000, "Assessment of Localized Deformation in Sand Using X-Ray Computed Tomography," *Geotech. Test. J.*, Vol. 23, No. 3, pp. 274–299.
- Arns, C. H., Knackstedt, M. A., Pinczewski, W. V., and Martys, N. S., 2004, "Virtual Permeametry on Microtomographic Images," *J. Petroleum Sci. Eng.*, Vol. 45, Nos. 1–2, pp. 41–44.
- Aste, T., Saadatfar, M., Sakellariou, A., and Senden, T. J., 2004, "Investigating the Geometrical Structure of Disordered Sphere Packings," *Physica A*, Vol. 339, pp. 16–23.
- ASTM D422-63, 2007, "Standard Test Method for Particle-Size Analysis of Soils," *Annual Book of ASTM Standards.*, Vol. 04.08, ASTM International, West Conshohocken, PA.
- ASTM D854-10, 2010, "Standard Test Methods for Specific Gravity of Soil Solids by Water Pycnometer," *Annual Book of ASTM Standards.*, Vol. 04.08, ASTM International, West Conshohocken, PA.
- Bhattad, P., Willson, C. S., and Thompson, K. E., 2010, "Segmentation of Low-Contrast Three-Phase X-Ray Computed Tomography Images of Porous Media," *Proceedings of the GeoX 2010: 3rd International Workshop on X-Ray CT for*

- Geomaterials*, New Orleans, LA, March 1–3, 2010, K. Alshibli and A. H. Reed, Eds., ISTE Ltd, London, UK and John Wiley & Sons Inc., Hoboken, NJ, pp. 254–261.
- Bhattad, P., Willson, C. S., and Thompson, K. E., 2011, “Effect of Network Structure on Characterization and Flow Modeling Using X-Ray Micro-Tomography Images of Granular and Fibrous Porous Media,” *Trans. Porous Media*, Vol. 90, No. 2, pp. 363–391.
- Bryant, S. and Blunt, M., 1992, “Prediction of Relative Permeability in Simple Porous Media,” *Phys. Rev. A*, Vol. 46, pp. 2004–2011.
- Bryant, S., Mellor, D., and Cade C., 1993, “Physically Representative Network Models of Transport in Porous Media,” *Aiche J.*, Vol. 39, No. 3, pp. 387–396.
- Culligan, K. A., Wildenschild, D., Christensen, B. S. B., Gray, W. G., and Rivers, M. L., 2006, “Pore-Scale Characteristics of Multi-phase Flow in Porous Media: A Comparison of Air–Water and Oil–Water Experiments,” *Adv. Water Res.*, Vol. 29, pp. 227–238.
- Dalla, E., Hilpert, M., and Miller, C., 2002, “Computation of the Interfacial Area for Two-Fluid Porous Medium Systems,” *J. Contam. Hydrol.*, Vol. 56, pp. 25–48.
- Desruses, J., Chambon, R., Mokni, M., and Mazerolle, F., 1996, “Void Ratio Evolution Inside Shear Bands in Triaxial Sand Specimen Studied by Computed Tomography,” *Geotechnique*, Vol. 46, No. 3, pp. 529–546.
- Diamond, S., 1970, “Pore Size Distributions in Clays,” *Clays Clay Miner.*, Vol. 18, pp. 7–23.
- Gladkikh, M. and Bryant, S., 2003, “Prediction of Interfacial Areas during Imbibition in Simple Porous Media,” *Adv. Water Res.*, Vol. 26, No. 6, pp. 609–622.
- Gladkikh, M. and Bryant, S., 2005, “Prediction of Imbibition in Unconsolidated Granular Materials,” *J. Colloid Interface Sci.*, Vol. 288, No. 2, pp. 526–539.
- Gladkikh, M. and Bryant, S., 2007, “Prediction of Imbibition from Grain-Scale Interface Movement,” *Adv. Water Res.*, Vol. 30, No. 2, pp. 249–260.
- Johns, R. A., Steude, J. S., Castanier, L. M., and Roberts, P. V., 1993, “Nondestructive Measurements of Fracture Aperture in Crystallite Rock Cores Using X-Ray Computed Tomography,” *J. Geophys. Res.*, Vol. 98, No. B2, pp. 1889–1900.
- Ketcham, R. A., 2005, “Forward and Inverse Modeling of low-Temperature Thermochronometry Data,” *Rev. Mineral. Geochim.*, Vol. 58, No. 1, pp. 275–314.
- Ketcham, R. A. and Carlson, W. D., 2001, “Acquisition, Optimization and Interpretation of X-Ray Computed Tomographic Imagery: Applications to the Geosciences,” *Comput. Geosci.*, Vol. 27, No. 4, pp. 381–400.
- Likos, W. J. and Lu, N., 2004, “Hysteresis of Capillary Stress in Unsaturated Granular Soil,” *J. Eng. Mech.*, Vol. 130, No. 6, pp. 646–655.
- Lindquist, W. B., Lee, S. M., Oh, W., Venkatarangan, A. B., Shin, H., and Prodanovic, M., 2005, *3DMA-Rock: A Software Package for Automated Analysis of Rock Pore Structure in 3-D Computed Microtomography Images*, SUNY, Stony Brook.
- Lu, N. and Likos, W. J., 2004, *Unsaturated Soil Mechanics*, Wiley, New York.
- Lu, N. and Likos, W. J., 2006, “Suction Stress Characteristic Curve for Unsaturated Soils,” *J. Geotech. Geoenviron. Eng.*, Vol. 132, No. 2, pp. 131–142.
- Lu, N., Wu, B., and Tan, C. P., 2007, “Tensile Strength Characteristics of Unsaturated Sands,” *J. Geotech. Geoenviron. Eng.*, Vol. 44, pp. 144–154.
- Lu, N., Kim, T. H., Sture, S., and Likos, W. J., 2009, “Tensile Strength of Unsaturated Sand,” *J. Eng. Mech.*, Vol. 135, No. 2, pp. 1410–1419.
- Lu, N., Godt, J. W., and Wu, D. T., 2010a, “A Closed-Form Equation for Effective Stress in Unsaturated Soils,” *Water Res. Res.*, Vol. 46.
- Lu, N., Zeidman, B., Wu, D. T., and Willson, C. S., 2010b, “Monte Carlo Simulation of Capillarity in Porous Materials,” *Geophys. Res. Lett.*, Vol. 37, p. L23402.
- Masad, E., Jandhyala, V. K., Dasgupta, N., Somedavan, N., and Shashidhar, N., 2002, “Characterization of Air Void Distribution in Asphalt Mixes Using X-Ray Computerized Tomography,” *J. Mater. Civil Eng.*, Vol. 14, No. 2, pp. 122–129.
- Oda, M., Takemiura, T., and Takahashi, M., “Microstructure in Shear Band Observed by Microfocus X-Ray Computed Tomography,” *Geotechnique*, Vol. 54, No. 8, pp. 539–542.
- Oh, W. and Lindquist, B., 1999, “Image Thresholding by Indicator Kriging,” *Pattern Anal. Mach. Intell., IEEE Trans.*, Vol. 21, No. 7, pp. 590–602.
- Oren, P. E. and Bakke S., 2002, “Process Based Reconstruction of Sandstones and Prediction of Transport Properties,” *Trans. Porous Media*, Vol. 46, Nos. 2–3, pp. 311–343.
- Prodanović, M., Lindquist, W. B., and Seright, R. S., 2006, “Porous Structure and Fluid Partitioning in Polyethylene Cores from 3D X-Ray Microtomographic Imaging,” *J. Colloid Interface Sci.*, Vol. 298, pp. 282–297.
- Prodanović, M., Lindquist, W. B., and Seright, R. S., 2007, “3D Image-Based Characterization of Fluid Displacement in a Berea Core,” *Adv. Water Res.*, Vol. 30, No. 2, pp. 214–226.
- Reed, A. H., Thompson, K. E., Briggs, K., and Willson, C. S., 2010, “Physical Pore Properties and Grain Interactions of SAX04 Sands,” *J. Oceanic Eng., IEEE*, Vol. 35, No. 4, pp. 488–501.
- Reeves, P. C. and Celia, M. A., 1996, “A Functional Relationship between Capillary Pressure, Saturation, and Interfacial Area as Revealed by a Pore Scale Network Model,” *Water Res. Res.*, Vol. 32, pp. 2345–2358.
- Richard, P., Philippe, P., Barbe, F., Bourles, S., Thibault, X., and Bideau, D., 2003, “Analysis by X-Ray Microtomography of a Granular Packing Undergoing Compaction,” *Phys. Rev., E*, Vol. 68, No. 2, p. 020301.
- Romero, E. and Simms, P. H., 2008, “Microstructure Investigation in Unsaturated Soils: A Review with Special Attention to Contribution of Mercury Intrusion Porosimetry and Environmental Scanning Electron Microscopy,” *Geotech. Geol. Eng.*, Vol. 26, pp. 705–727.
- Schnaar, G. and Brusseau, M. L., 2005, “Pore-Scale Characterization of Organic Immiscible-Liquid Morphology in Natural Porous Media Using Synchrotron X-Ray Microtomography,” *Environ. Sci. Technol.*, Vol. 39, pp. 8403–8410.
- Seidler, G. T., Martinez, G., Seeley, L. H., Kim, K. H., Behne, E. A., Zaranek, S., Chapman, B. D., Heald, S. M., and Brewe, D. L., 2000, “Granule-by-Granule Reconstruction of a Sandpile from X-Ray Microtomography,” *Phys. Rev., E*, Vol. 62, No. 6, pp. 8175–8181.
- Silin, D. and Patzek, T., 2006, “Pore Space Morphology Analysis Using Maximal Inscribed Spheres,” *Phys. A: Stat. Theoret. Phys.*, Vol. 371, No. 2, pp. 336–360.
- Sridharan, A., Altschaeffl, A. G., and Diamond, S., 1971, “Pore Size Distribution Studies,” *J. Soil Mech. Found. Div., ASCE*, Vol. 97, No. 5, pp. 771–787.

- Thompson, K. E. and Fogler, H. S., 1997, "Pore-Level Mechanisms for Altering Multiphase Permeability with Gels," *SPE J.*, Vol. 2, No. 3, pp. 350–262.
- Thompson, K. E., Willson, C. S., and Zhang, W., 2006, "Quantitative Computer Reconstruction of Particulate Materials from Microtomography Images," *Powder Technol.*, Vol. 163, No. 3, pp. 169–182.
- Thompson, K. E., Willson, C. S., White, C. D., Nyman, S., Bhattacharya, J. P., and Reed, A. H., 2008, "Application of a New Grain-Based Algorithm to Microtomography Images for Quantitative Characterization and Flow Modeling," *J. Soc. Pet. Eng.*, Vol. 13, No. 2, pp. 164–176.
- van Genuchten, M. T., 1980, "A Closed Form Equation for Predicting the Hydraulic Conductivity of Unsaturated Soils," *Soil Sci. Soc. Am. J.*, Vol. 44, pp. 892–898.
- Verhelst, F., Vervoort, A. D. B., and Marchal, G., 1995, *X-Ray Computerized Tomography: Determination of Heterogeneities in Rock Samples*, Vol. 1, Balkema, Rotterdam, The Netherlands, pp. 105–109.
- Wang, L. B., Frost, J. D., and Lai, J. S., 2004, "Three-Dimensional Digital Representation of Granular Material Microstructure from X-Ray Tomography Imaging," *J. Comput. Civil Eng.*, Vol. 18, No. 1, pp. 28–35.
- Wildenschild, D., Hopmans, J. W., Vaz, C. M. P., Rivers, M. L., and Rikard, D., 2002, "Using X-Ray Computed Tomography in Hydrology: Systems, Resolutions, and Limitations," *J. Hydrol.*, Vol. 267, Nos. 3–4, pp. 285–297.
- Wildenschild, D., Hopmans, J. W., Kent, A. J. R., and Rivers, M. L., 2005, "A Quantitative Study of Flow-Rate Dependent Processes Using X-Ray Microtomography," *Vadose Zone J.*, Vol. 4, pp. 112–126.